Ultraviolet supercontinuum generation using a differentially-pumped integrated glass chip

Journal of Physics: Photonics

PAPER

Ultraviolet supercontinuum generation using a differentially-pumped integrated glass chip

Vincent Wanie[1,7,*], Pasquale Barbato[2,6,7], Josina Hahne[3,4,7], Sergey Ryabchuk[3,4], Ammar Bin Wahid[1], David Amorim[1], Erik P Månsson[1], Andrea Trabattoni[1,5], Roberto Osellame[6], Rebeca Martínez Vázquez[6] and Francesca Calegari[1,3,4]

[1] Center for Free-Electron Laser Science CFEL, Deutsches Elektronen-Synchrotron DESY, Notkestr. 85, 22607 Hamburg, Germany
[2] Department of Physics, Politecnico di Milano, Piazza L. da Vinci 32, 20133 Milano, Italy
[3] Department of Physics, Universität Hamburg, Luruper Chaussee 149, 22761 Hamburg, Germany
[4] The Hamburg Centre for Ultrafast Imaging, Luruper Chaussee 149, 22761 Hamburg, Germany
[5] Institute of Quantum Optics, Leibniz Universität Hannover, Welfengarten 1, 30167 Hannover, Germany
[6] Institute for Photonics and Nanotechnologies CNR-IFN, P.za L. da Vinci 32, 20133 Milano, Italy
[7] These authors contributed equally to this work.
[*] Author to whom any correspondence should be addressed.

E-mail: vincent.wanie@desy.de

OPEN ACCESS

RECEIVED
20 October 2023

REVISED
8 February 2024

ACCEPTED FOR PUBLICATION
21 February 2024

PUBLISHED
7 March 2024

Keywords: ultraviolet radiation, third-harmonic generation, frequency conversion, ultrafast optics, femtosecond laser micromachining, differential pumping, ultrafast UV spectroscopy

Supplementary material for this article is available online

Abstract

We investigate the generation of ultrabroadband femtosecond ultraviolet (UV) radiation via third-order harmonic generation in highly confined gas media. A dual-stage differential-pumping scheme integrated into a glass microfluidic chip provides an exceptional gas confinement up to several bar and allows the apparatus to be operated under high-vacuum environment. UV pulses are generated both in argon and neon with up to $\sim$0.8 μJ energy and 0.2% conversion efficiency for spectra that cover the UVB and UVC regions between 200 and 325 nm. Numerical simulations based on the unidirectional pulse propagation equation reveal that ionization plays a critical role for extending the spectral bandwidth of the generated third-harmonic pulse beyond the tripled 800 nm driving laser pulse bandwidth. By delivering UV supercontinua supporting Fourier transform limits below 2 fs, as well as comparable pulse energies with respect to capillary-based techniques that typically provide high spectral tunability but produce narrower bandwidths, our compact device makes a step forward towards the production and application of sub-fs UV pulses for the investigation of electron dynamics in neutral molecules.

1. Introduction

Advancements in laser technology have recently enabled the development of intense and coherent ultraviolet (UV) light sources, opening up a variety of opportunities to conduct scientific research aiming to address fundamental questions of relevance in fields such as biology and atmospheric chemistry. Particularly, several phenomena occurring in nature involve the UV-excited dynamics of valence shell electrons in molecules, which are ultimately responsible for bond formation and breaking and therefore for the chemical changes that occur at longer time scales [1]. In this context, the engineering of novel UV light sources is constantly evolving towards the generation of temporally shorter and shorter light pulses with few-femtosecond duration [2]. While challenging, this provides new tools to harness unachieved temporal resolutions that are necessary for the real-time mapping of the fastest dynamical changes of matter following UV-excitation.

Narrowband UV pulses can be produced via frequency up-conversion from picosecond lasers. Standard schemes employ cascaded sum-frequency generation in nonlinear crystals and can result in conversion efficiencies as high as 80% at a central wavelength near 350 nm [3]. The use of femtosecond lasers significantly pushed forward the achievable bandwidth supporting pulses below 10 fs. Record temporal

duration using nonlinear crystals has been obtained via achromatic second harmonic generation with a careful manipulation of the resulting spectral phase using deformable mirrors, delivering a UVB bandwidth spanning from 290 to 310 nm and supporting a Fourier transform limit (TL) of 6.4 fs [4]. Other examples include the generation of 8.4 fs UVA pulses (320–370 nm) via indirect phase transfer [5] during the sum-frequency generation of a non-collinear optical parametric amplifier [6]. Further reduction of the pulse duration is hard to achieve with nonlinear crystals because of the limited phase matching conditions and the highly dispersive properties of materials for ultrabroadband UV radiation.

The production of even broader UV supercontinua in the UVB and UVC typically requires using quasi dispersion-free gas media for the nonlinear interaction. The use of 800 nm multi-cycle femtosecond pulses to drive UV resonant dispersive wave emission in the fundamental or even the higher-order modes of gas-filled hollow capillary fibers [7–10], or few-cycle pulses for driving third-harmonic generation (THG) in quasi-static gas cells [11] has enabled to break the 3 fs barrier. Conventional metal cells are quite sensitive to the high intensities of the driving laser that must interact with the gas and thus their entrance and exit are prone to being ablated during experiments, with the consequence of modifying generation conditions and thus the stability of the UV radiation. We recently demonstrated how a differential-pumping scheme made of a three sub-chambers assembly, in which a few-mm glass cell is embedded, can efficiently extract the residual gas that is expelled from the highly pressurized region of the cell and confine THG over a few millimeters [12]. Due to the high resistivity of glass to the laser intensity, the stability of the setup allowed us to track in real-time the UV-induced electron dynamics of chiral molecules with unprecedented time resolution [13].

Here, we report on the design and performance of a novel integrated glass chip incorporating a UV generation cell with two laser-micromachined differential pumping stages. By focusing few-cycle, near-infrared (NIR) pulses into its central compartment, operated at multi-bar pressures, we produce UV supercontinua in noble gases through third-order nonlinearities. The use of an integrated dual-stage differential-pumping scheme results in enhanced conversion efficiencies, leading to near-microjoule pulse energy for spectral bandwidths covering both UVB and UVC and resulting in transform limited pulse durations below 2 fs. The compactness of the device in which the glass chip is embedded makes it a versatile tool that can be easily implemented into attosecond beamlines that are typically operating in vacuum for ultrafast spectroscopic applications.

2. Experimental setup

A titanium:sapphire laser producing 25 fs pulses at 800 nm central wavelength is spectrally broadened using a 2.3 m long hollow-core fiber filled with a gradient of helium gas. Chirped mirrors are used to compress the outgoing pulses, which are sent to the experimental setup shown in figure 1(a). Briefly, the NIR intensity is controlled with a broadband half-waveplate and a silicon mirror placed at Brewster angle. The dispersion is controlled with a SiO_2 wedge pair and 6.1 fs pulses are characterized by second-harmonic frequency-resolved optical gating [14]. The beam is transported into a vacuum chamber and is focused ($f = 70$ cm) at the center of the differentially-pumped integrated glass chip to a waist of 65 μm ($1/e^2$). The UV pulses produced via THG exit the vacuum chamber through an anti-reflection coated fused silica window. The residual NIR radiation is completely filtered out using four spectral separators from Layertech [reflectivity (230 nm–330 nm) $\approx$ 95% and reflectivity (380 nm–800 nm) $<$5%]. The pulse energy was measured with a Gigahertz-Optik optometer (ISD-5P-SiUV) and spectra were acquired with an Ocean Insight spectrometer (OCEAN-FX-XR1-ES).

The differential-pumping chip used for the experiment is shown in figure 1(b). It consists in a $15 \times 49 \times 3$ mm^3 SiO_2 slab machined by femtosecond laser irradiation followed by chemical etching (FLICE) [15]. The central part contains a 3 mm long cell with a 500 μm diameter at the center that reduces towards the extremities to 400 μm [12]. Two differential-pumping stages are integrated on each side of the cell within the chip, characterized by 10×6 mm^2 rectangular shaped cavities (blue shaded volumes). On the wider surface, a gas inlet is engraved at the center and connects to the gas reservoir. Additional details about the fabrication of the glass chip are provided in appendix A. The chip is mounted onto an assembly block that is used for connecting the four pumping channels. Flexible tubing allows the entire unit to be moved for alignment around the laser beam by using a 5-axis motorized stage that is mounted underneath the block (see appendix A). With a total length of about 10 cm, the overall setup is extremely compact and can therefore be easily mounted into various experimental setups.

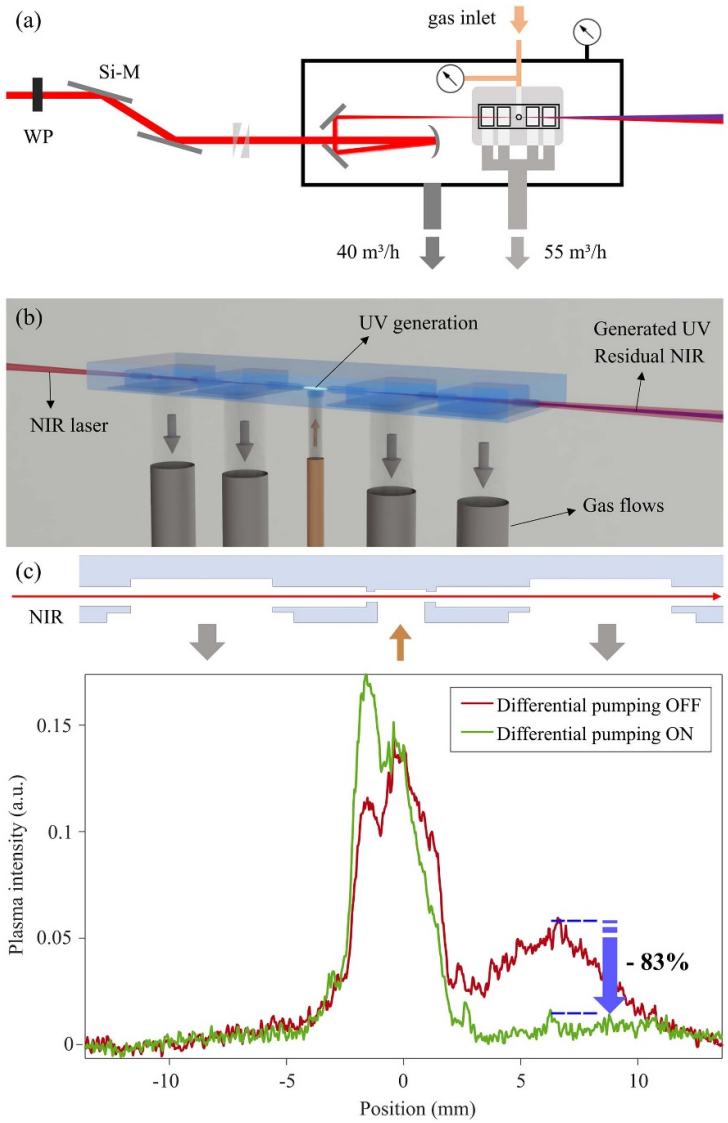

Figure 1. (a) Sketch of the experimental setup. Intensity regulation of a 800 nm NIR driving field is performed using a half-waveplate (WP) and a silicon mirror (Si-M) at Brewster angle. A fused silica wedge pair is used to adjust the dispersion. The UV generation section includes a vacuum chamber where the NIR beam is focussed into the center of the differentially-pumped integrated glass chip. The main chamber is evacuated by a 40 $m^3\ h^{-1}$ multi-stage roots pump, while the chip is evacuated using a 55 $m^3\ h^{-1}$ pump. (b) Graphical representation of the chip. Gas is injected into the central generation cell of the chip, where it interacts with the NIR driving field, producing UV pulses through third-harmonic generation. Simultaneously, the gas is evacuated via four differential-pumping chambers to prevent reabsorption of the generated UV radiation. (c) On-axis profile of the plasma intensity measured in 0.25 bar of argon with the differential pumping on and off. When the differential pumping is turned on, THG takes place between −2.5 and 2.5 mm and the secondary intensity peak at about 5 mm is drastically reduced, preventing the reabsorption of the UV radiation.

3. Experimental results

3.1. Differential pumping performances

To evaluate the gas confinement enabled by the differentially-pumped integrated glass chip, we imaged the profile of the plasma fluorescence along the cell length that is emitted as a function of argon pressure interacting with a NIR pulse at an intensity of 1.9×10^{14} W cm^{-2} [16]. Details about the measurements can be found in appendix B. The comparison when switching the differential pumping respectively off and on for a pressure of 0.25 bar is shown in figure 1(c). When differential pumping is turned off and the gas evacuation relies only on the pump that is connected to the main vacuum chamber, a non-negligible amount of gas is still present on either side of the highly pressurized central section. In such case, the UV radiation that is produced ionizes the gas media after the generation cell, leading to the asymmetric profile. This partial re-absorption of the UV radiation has a detrimental effect on the conversion efficiency. When differential pumping is turned on, we observe a drastic reduction, greater than 80%, in the intensity of the secondary plasma. This effect leads to enhanced conversion efficiencies for the THG, as will be reported below. The

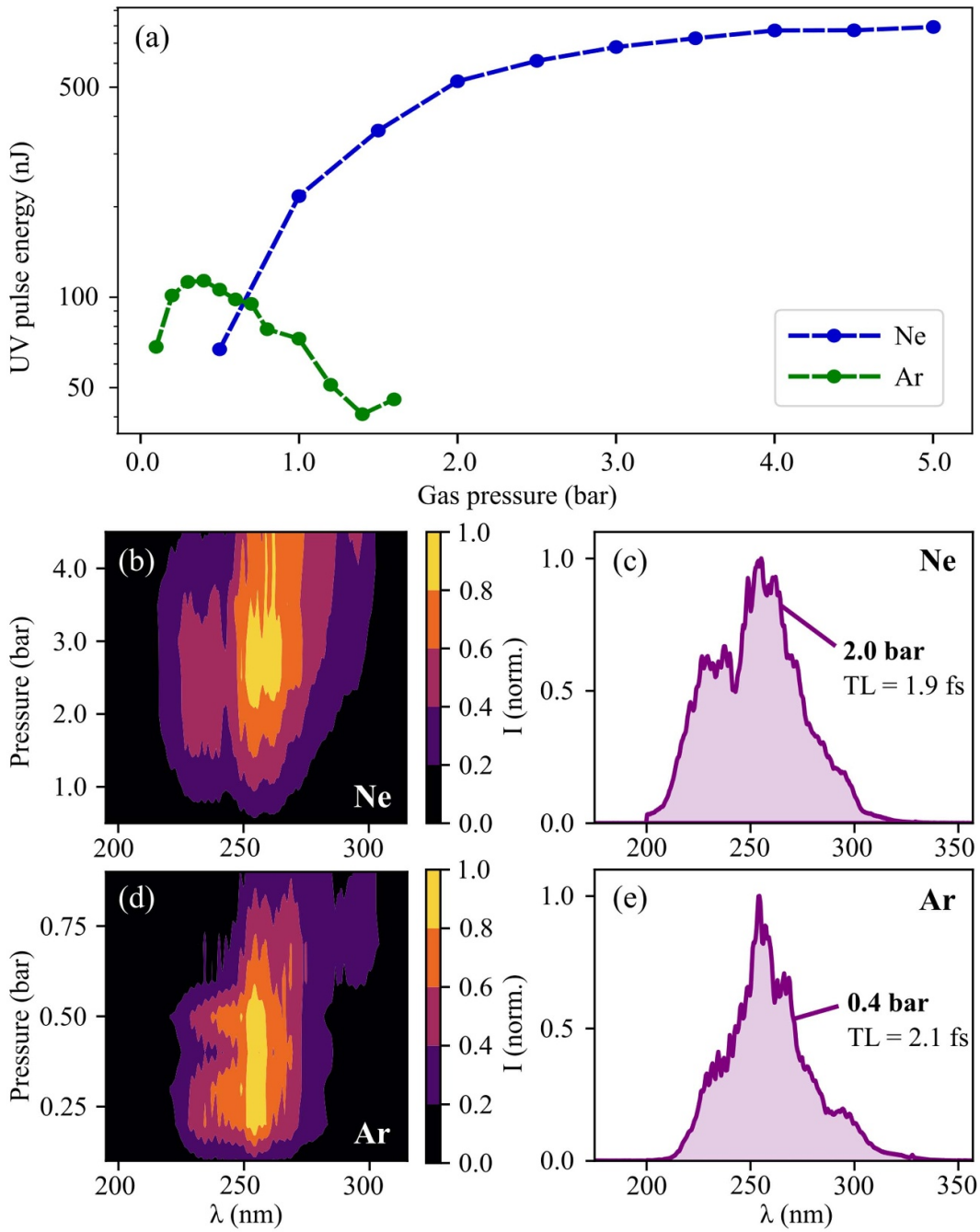

Figure 2. Experimental results. (a) Scaling of the UV pulse energy at the generation point as a function of gas pressure. (b) Spectral broadening as a function of neon gas pressure. (c) Broadest spectra obtained in 2.0 bar of neon before spatial distortion of the UV beam profile occurs. (d) Spectral broadening as a function of argon gas pressure. (e) Broadest spectra obtained in 0.4 bar of argon before spatial distortion of the UV beam profile occurs.

variation in plasma intensity for the central section cannot be quantitively interpreted because the response is not linear in this highly pressurized region, as shown in the calibration curve of appendix B. The overall performance of the integrated differential pumping scheme allows us to reach a base vacuum level of about 1.1×10^{-1} mbar when up to 5 bar of argon gas is injected into the cell.

3.2. UV generation

Figure 2(a) shows how the UV pulse energy scales with respect to the argon and neon gas pressure when driving THG at NIR intensities of 3.5×10^{14} and 9.3×10^{14} W cm^{-2}, respectively. Results from tuning the fundamental NIR to other intensities—corresponding to inferior performances according to our criteria discussed below—are provided in the supplement material (SM). In argon, saturation is observed at 0.4 bar with an energy per pulse of 115 nJ at the generation point, taking into account the overall reflectivity of our optical setup. With a driving pulse energy of 150 μJ, a retrieved conversion efficiency of the THG process of

0.08% is comparable with previous measurements [12]. However, this saturation is reached at much lower gas pressures at similar peak intensities, thanks to the high confinement of the gas within the differential pumping chip shown in figure 1(c). In neon, no saturation is observed up to 5 bar where a plateau is reached. Higher pressures were not tested to avoid potential mechanical damage of the differential-pumping glass chip. Nevertheless, an exceptional pulse energy of ~0.8 μJ is obtained from a 400 μJ driving pulse, corresponding to 0.2% conversion efficiency, 2.5 times as high as in argon.

In figures 2(b) and (d), we show the corresponding evolution of the spectral broadening as a function of the neon and argon gas pressures. In neon (b), the spectrum initially exhibits a single peak centered at 260 nm. As the pressure is increased, a second peak appears at about 235 nm due to self-steepening and plasma-induced blue shifting of the driving field, as will later be shown from numerical simulations. Experimentally, it is observed that the generated UV experiences spatial beam distortions from 2.5 bar due to ionization, which also leads to the observed amplitude reduction of the 235 nm peak from this pressure on. In figure 2(c), we thus show the spectrum obtained for the best experimental conditions at 2 bar where the beam quality is preserved. The spectrum spanning from 200 nm to 325 nm supports a 1.9 fs duration. Note that the sharp cut at 200 nm is caused by the detection limit of our spectrometer.

In comparison, figure 2(d) shows the spectral evolution of argon. In this case the spectral broadening develops symmetrically and from 0.5 bar the overall spectral amplitude starts to decrease due to ionization. The spectral evolution takes place at lower gas pressures because of the lower ionization potential of argon and the best spectrum obtained without any spatial distortion of the beam is found at 0.4 bar, shown in figure 2(e), spanning from 220 nm to 325 nm with a TL of 2.1 fs.

4. Numerical simulations

To gain further insights into the experimental observations and the effect of critical parameters for the UV generation, we performed simulations by solving the unidirectional pulse propagation equation [17] using the propagation solver *Luna.jl* [18, 19]:

$$\frac{\partial}{\partial z}\mathbf{E}(\omega,\mathbf{k}_\perp,z)=\mathcal{L}(\omega,z)\,\mathbf{E}(\omega,\mathbf{k}_\perp,z)+\frac{i\omega}{N}\mathbf{P}^{\mathrm{NL}}(\omega,\mathbf{k}_\perp,z) \tag{1}$$

where $\mathbf{E}(\omega,\mathbf{k}_\perp,z)$ is the reciprocal-space electric field amplitude, $\mathbf{k}_\perp$ is the transverse spatial frequency vector, $\mathcal{L}(\omega,z)$ is a linear operator describing dispersion and absorption, $\mathbf{P}^{\mathrm{NL}}(\omega,\mathbf{k}_\perp,z)$ is the nonlinear polarization in reciprocal space and N is a normalization factor.

The nonlinear polarization includes all third-order nonlinearities, as well as photionization of the gas medium described as [20]:

$$\frac{\partial}{\partial t}\mathbf{P}^{\mathrm{ion}}(t,\mathbf{r})=\frac{I_p}{\mathbf{E}(t)}\frac{\partial n_e}{\partial t}+\frac{e^2}{m_e^2}\int_{-\infty}^{t}n_e(t')\,\mathbf{E}(t')\,dt' \tag{2}$$

where n_e(t) is the free electron density, I_p is the ionization potential, and e, m_e represent the electron charge and mass, respectively. $n_e(t)$ is obtained from

$$\frac{\partial n_e}{\partial t}=(n_e-n_0)\,W(\mathbf{E}) \tag{3}$$

where n_0 is the initial number of neutral atoms and $W(\mathbf{E})$ the ionization rate, calculated using the PPT model for both argon and neon [21, 22].

The free space propagation of both the driving NIR field and the generated UV supercontinuum is described by the linear operator $\mathcal{L}(\omega,z)$:

$$\mathcal{L}(\omega,z)=i\left(\beta(\omega,z)-\frac{\omega}{v}\right)-\frac{1}{2}\alpha(\omega,z) \tag{4}$$

where $\beta(\omega,z)$ is the propagation coefficient of the gas, v is the group velocity at the central wavelength λ_0 and $\alpha(\omega,z)$ is the absorption coefficient of the gas.

The gas distribution is described by the experimental fluorescence measurements at 0.15 bar of argon (see appendix B, figure B1(d)). Since the fluorescence signal does not scale linearly at higher pressures and thus may provide a less accurate description of the gas distribution in the central part of the cell for these cases, the 0.15 bar distribution was used for all simulations and scaled to variable peak pressures.

Figure 3(a) shows the simulated energy scaling of the UV pulses for both argon and neon (solid lines), reproducing well the experimental results (dashed lines). However, for both gases, the UV pulse energy is one order of magnitude larger than in the experiment. We assign this discrepancy to the regions outside the

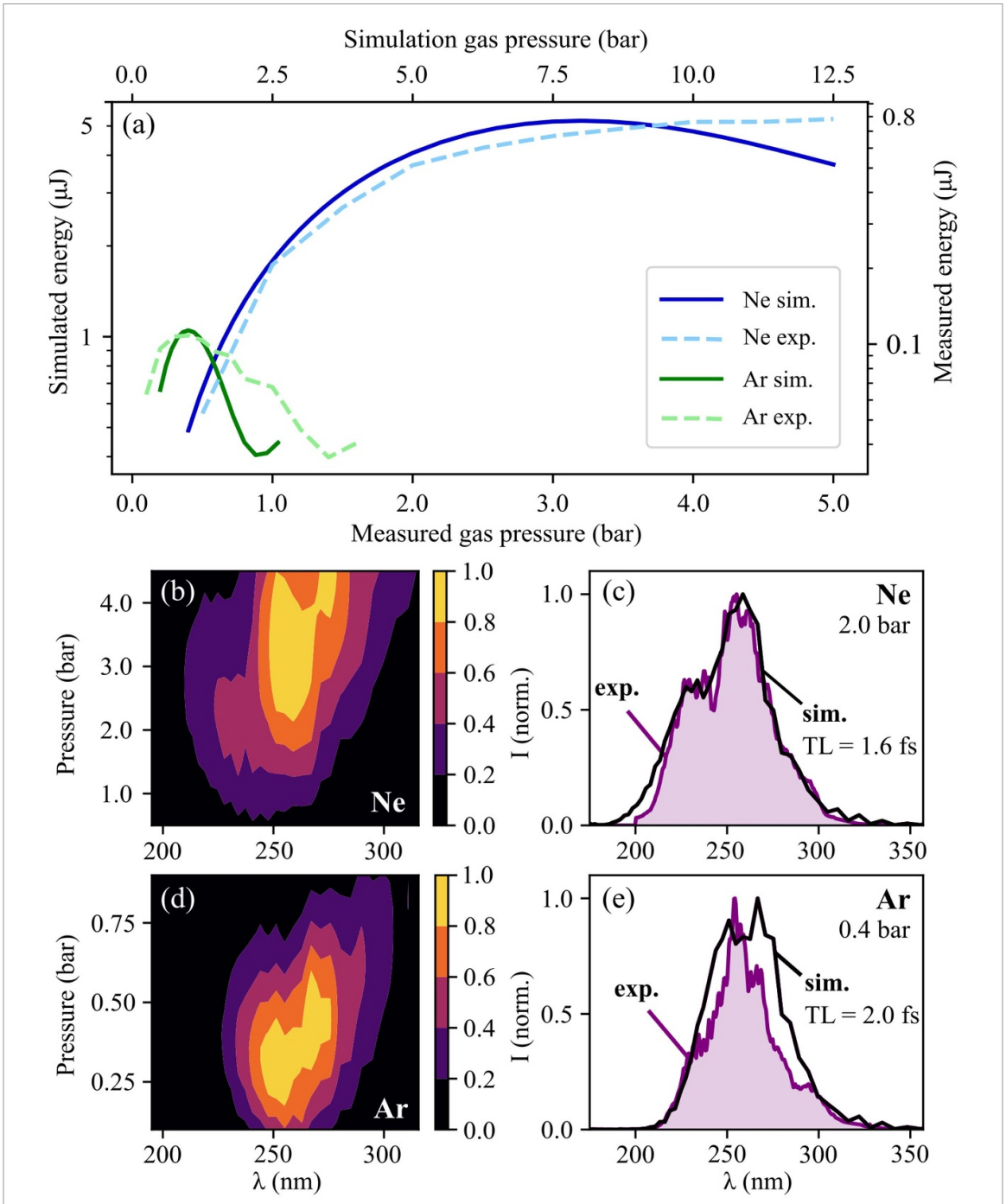

Figure 3. Simulated spectra after propagation in the 3 mm generation cell. (a) Scaling of the UV pulse energy as a function of gas pressure. The simulated UV pulse energy (solid lines, left axis) dependance on the simulation gas pressure (top axis) is compared to experimental results from figure 2(a) (dashed lines). For comparison with the experimental results, a rescaling factor 0.4 for the simulated pressure has been applied to all subsequent graphs (see main text). (b) Simulated spectral broadening as a function of neon gas pressure. (c) Simulated (black) and measured (purple) spectrum at 2.0 bar of neon. (d) Simulated spectral broadening as a function of argon gas pressure. (e) Simulated (black) and measured (purple) spectrum at 0.4 bar of argon.

generation cell—not taken into account in our simulations—where partial absorption of the UV radiation takes place. These regions also result in pressures which are about 2.5 times higher in the simulation (top axis in figure 3(a)) compared to the experiment (bottom axis). We show in the SM how the selected interaction length affects the simulations. Nevertheless, as will be shown below, the spectral evolution for each gas is well reproduced and thus a common multiplication factor of 0.4 was applied to both simulated curves in order to match the experimental pressure and facilitate our qualitative comparison. Figures 3(b) and (d) shows the corresponding simulated spectral evolution of the UV supercontinua as a function of the rescaled gas pressure. The main features observed experimentally are reproduced by the model: in neon (b) the spectrum develops over two main peaks at about 250 and 235 nm and the spectra support TL durations down to 1.6 fs (c). In argon (d), symmetric broadening centered at about 250 nm is observed until 0.4 bar at which a TL of

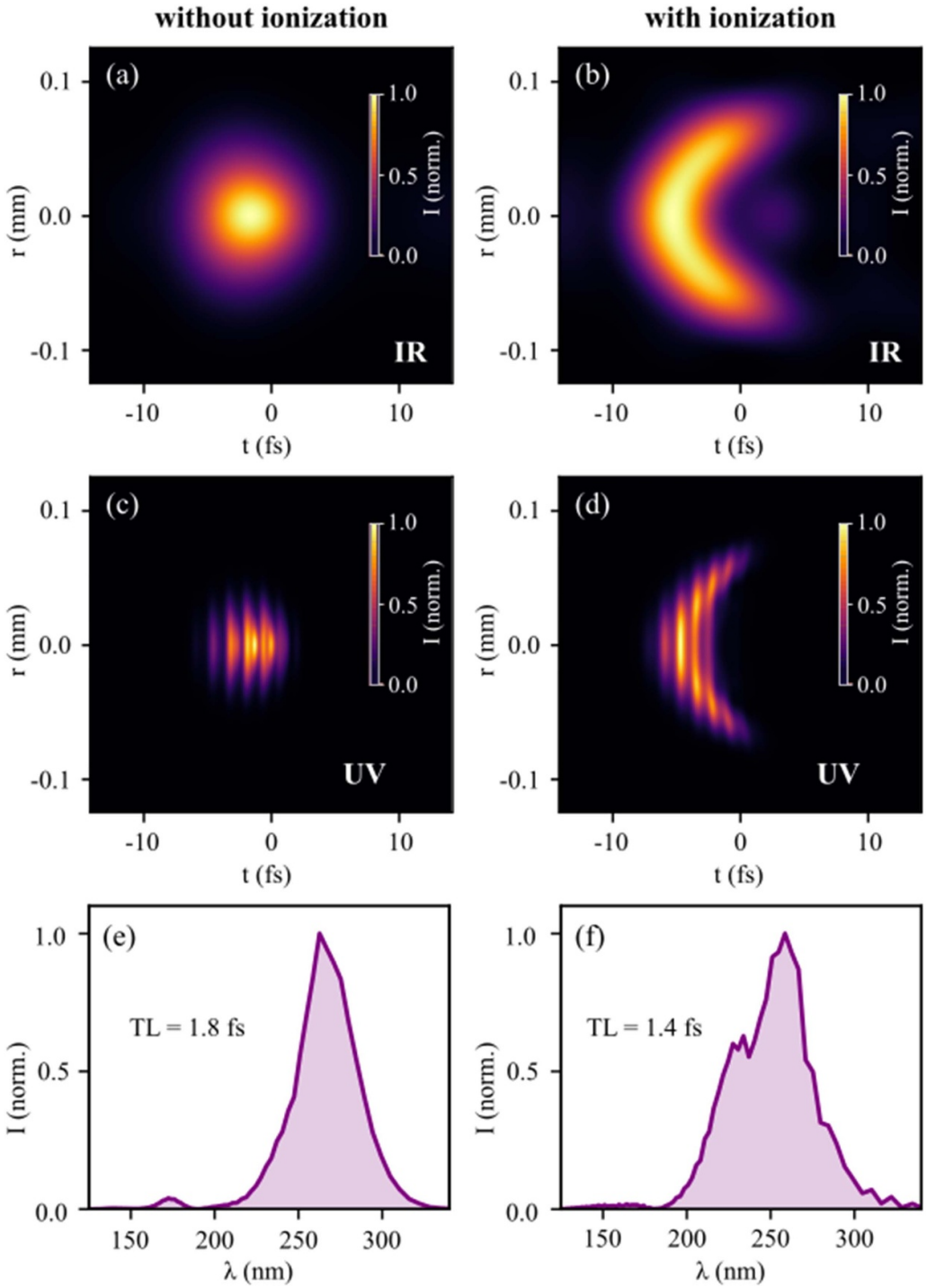

Figure 4. Propagation simulations after the 3 mm generation cell filled with 2.0 bar of neon gas. (a), (b) Comparison of the spatio-temporal properties of the NIR driving field when ionization is disabled or enabled, respectively. The trailing edge of the pulse experiences self-defocusing when ionization occurs. (c), (d) Spatio-temporal properties of the UV pulse. Ionization confines the UV generation mainly to the rising edge of the corresponding NIR driving pulse. (e), (f) Spectral content of the UV pulse when ionization is disabled or enabled, respectively. Ionization leads to a significant extension of the spectral content via plasma blue shifting, decreasing the TL duration from 1.8 fs to 1.4 fs.

2.0 fs is obtained (e). For higher pressures, the spectral broadening at 270 nm originates from pure THG and, in contrast to the contribution at 250 nm, remains when ionization effects, discussed below, are not taken into account. Additional results can be found in the SM (figure S5), further supporting the agreement between simulation and experiment at other pressures.

The simulations allow us to further investigate parameters which are not easily accessible experimentally. In figure 4, we show how ionization of the gas medium affects the spatio-temporal properties of both the driving NIR field (a)–(b) and the generated UV pulses (c)–(d) after 3 mm propagation in 2 bar of neon. By

turning off the ionization (a), the NIR field preserves a nearly symmetric profile along the time axis, leading to a homogeneous THG over the entire pulse envelope. The resulting spectrum in figure 4(e) also displays a symmetric profile supporting a TL of 1.8 fs, shorter than the duration expected from pure THG, i.e. $1/\sqrt{3}$ of the 6.1 fs NIR driving pulse. We assign the additional spectral broadening to self-phase modulation and wave mixing processes which also take place within the highly pressurized gas cell, as observed below 200 nm. These additional processes also lead to the temporal modulation of the UV spatio-temporal profiles in figures 4(c) and (d). Instead, the plasma produced by ionization leads to a defocusing of the NIR pulse trailing edge in figure 4(b), confining the UV generation mainly to the leading edge (d). This spatio-temporal reshaping and the self-steepening experienced by the driving field leads to further spectral broadening, producing a spectrum supporting an exceptional TL of 1.4 fs in figure 4(f). This observation is in agreement with previously performed calculations that have predicted similar effects [23]. The shorter TL duration compared to figure 3(c) is due to the wave mixing contribution at 160 nm. This spectral region has been omitted in figure 3(c) to allow for a direct comparison with the experiment where wavelengths below 200 nm were not detected.

5. Conclusions

We have reported the design and performances of a novel device for the production of near octave-spanning UV supercontinua through third-order nonlinearities in gases. A dual-stage differential pumping scheme integrated into a glass microfluidic chip leads to high confinement of multi-bar gas pressure and conversion efficiencies up to 0.2%, providing ~0.8 μJ/pulse in neon. Due to a better management of the outflowing gas using our integrated differential-pumping scheme, this energy is over two times higher than what could be achieved by using our previous glass chip design [12]. Using numerical simulations we discussed the impact of the gas pressure and ionization effects on the spectral and temporal properties of the generated UV pulses. It was found that ionization is essential to enlarge the spectral bandwidth between 200–325 nm in order to support TL durations below 2 fs. By exploring a series of gas distributions through simulations, additional modifications to the cell geometry could further improve the conversion efficiency.

To the best of our knowledge, this is the first time that a differentially-pumped integrated glass chip is presented and used to generate coherent and ultrashort UV laser light in a high-density gas cell while maintaining a good vacuum level in the main chamber. The fabrication of the device is challenging as it combines mm-size features such as the pumping chambers with μm-size structures such as the connecting channels and the generation cell. However, thanks to the versatility of the FLICE technique these μm-size structures can be easily modified to tailor specific focusing conditions or gas densities. The compactness and the provided gas-extinction efficiency of the device allows for its implementation into various beamlines operating under high-vacuum conditions. These features will benefit other nonlinear applications that rely on precise gas density control and micrometer structures, such as high-harmonic generation for the production of attosecond light pulses [24]. The dispersion-free nature of the method enables high temporal resolution for time-resolved spectroscopic applications employing UV pulses and we foresee that driving our device with near single-cycle NIR pulses has the potential to experimentally break the sub-fs barrier for UV radiation.

Data availability statements

The data that support the findings of this study are available upon reasonable request from the authors.

Acknowledgments

We are thankful to Christian Brahms for helpful discussions regarding the *Luna.jl* propagation solver. This work was funded by the European Research Council under the ERC-2014-StG STARLIGHT (Grant No. 637756), the Cluster of Excellence 'CUI: Advanced Imaging of Matter' of the Deutsche Forschungsgemeinschaft (DFG)—EXC 2056—project ID 390715994, the DFG—SFB-925—Project ID 170620586, the Helmoltz-Lund International Graduate School (HELIOS) and the European Union's Horizon 2020 Research and Innovation Program under the Grant Agreement No. 964588 (XPIC). V W acknowledges support from the Partnership for Innovation, Education and Research (PIER) (PIF-2021-03). A T acknowledges support from the Helmholtz association under the Helmholtz Young Investigator Group VH-NG-1603.

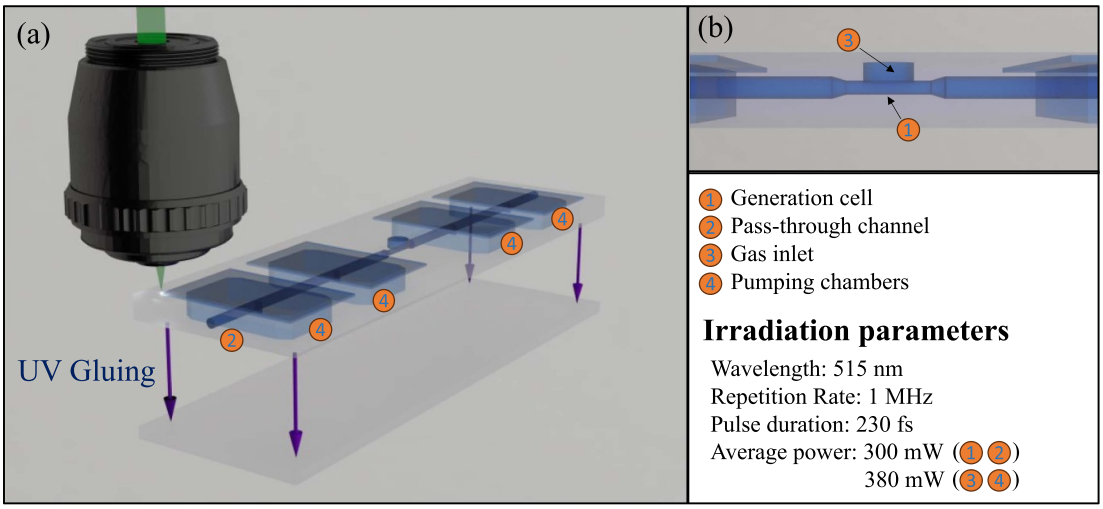

Figure A1. (a) Graphical representation of the fabrication procedure and (b) a close up of the generation cell.

Appendix A. Glass chip fabrication

The distinctive feature of the differentially-pumped integrated glass chip lies in its design to host high-intensity-driven nonlinear interactions while ensuring an optimal gas distribution. This goal has been achieved thanks to hollow three-dimensional structures (namely: the central cell, devoted to the UV generation, the gas inlet, the pumping chambers for the gas evacuation, and the pass-through channel for the laser propagation). The chip is fabricated in fused silica, a material that guarantees a minimal gas permeability together with an excellent mechanical and chemical stability. The hollow structures network is manufactured through Femtosecond Laser Irradiation followed by Chemical Etching (FLICE), a two-step microfabrication technique for the realization of hollow structures embedded within the SiO_2 glass, whose dimensions can range from hundreds of nanometers to centimeters [15]. FLICE is based on the absorption of a visible or infrared train of laser pulses tightly focused inside the material. While silica is generally transparent at these wavelengths, the fluence in the focal volume is sufficient to promote nonlinear absorption phenomena that lead to a permanent modification of the substrate. The modified region is subsequently selectively etched by a chemical agent in what constitutes the second step of the process.

The irradiation of the glass chip was performed on a $49 \times 15 \times 2$ mm^3 fused silica slab (Corning HPFS 7980 Standard Grade). Although it would have been possible to realize a monolithic device, it was decided to microstructure a 2 mm-thick sample and subsequently use a UV adhesive to glue it on a 1 mm-thick slab of the same material to simplify the process and reduce the overall irradiation time (figure A1). In this way it was possible to avoid irradiating chamber floors, which, given their size, would have added many hours of processing time. In any case, it should be noted that the generation cell in the center, the most critical structure of the whole device, is fully integrated into the main glass slab, thus ensuring a perfect sealing.

The beam was provided by a femtosecond Yb-doped fiber laser (Satsuma, Amplitude Systems S.A.), that delivered 260 fs pulses at a central wavelength of 1030 nm and a repetition rate of 1 MHz. The wavelength was frequency doubled to 515 nm with an LBO crystal and the beam was directed to a microscope 63*X* dry objective (Zeiss, LD-plan Neofluor, NA = 0.65) which focuses the beam inside the substrate. The objective is equipped with a correction collar to compensate spherical aberrations, the position of which was changed once during the fabrication to ensure the maximum laser focal spot uniformity within the substrate depth. The sample is mounted on a 2D stage (Aerotech, ANT95-50-XY-CMS-ULTRA) for the movement in the *XY* plane while the objective is affixed to a pneumatic 1D translational stage (Aerotech, ANT130-035-L-ZS-PLUS), allowing the translation of the focus on the *Z* axis. This configuration enables the movement of the laser focus with respect to the sample and thus makes it possible to irradiate the profile of the glass chip with nanometric precision, which is illustrated in figure A1. The first structure to be irradiated was the generation cell, its connection with the pass-through channel (figure A1(b)) and the straight connecting channel over the full 49 mm chip length, with an average power of 300 mW. Then, the gas inlet and the pumping chambers were inscribed with an average power of 380 mW. The overall duration of the irradiation was about 22 h.

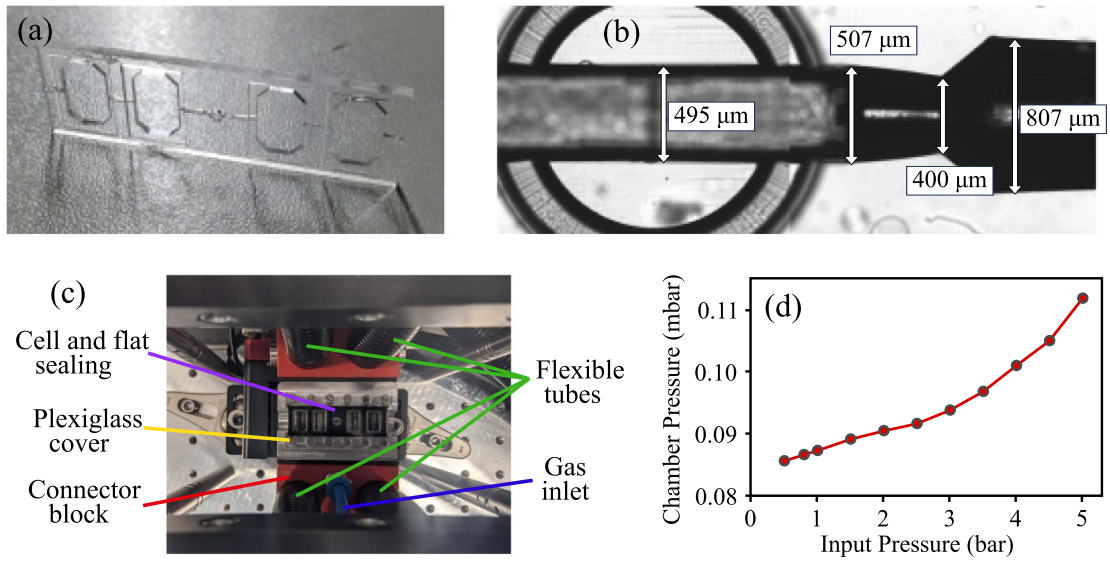

Figure A2. (a) Picture of the laser-micromachined structure before gluing. (b) Composite image taken with an optical microscope, providing a detailed view of the chip and its connection with the channel. (c) Picture of the differential-pumping integrated glass chip positioned inside the vacuum chamber with the connection system to the vacuum pumps and gas inlet. (d) Pressure measured in the main vacuum chamber for different input pressures at the cell.

The second step of the process consisted in the chemical etching in a 20% hydrogen fluoride (HF) aqueous solution using an ultrasonic bath at a controlled temperature of 35 °C for 10 h. The solution was refreshed after the first 5 h. The gas inlet, the pumping chambers and the lateral accesses served as entrances for the HF solution, which eventually reached all the irradiated areas, emptying them from the glass and leaving behind hollow structures in the shapes and dimensions specified by the design. A picture of the device at this stage is shown in figure A2(a).

After the etching, the sample was kept for 30 min in an isopropyl alcohol ultrasonic bath for removing any residual impurity from the inner structures. An additional cleaning step of the two surfaces to be bonded was performed with an O_2 plasma cleaner (Diener Zepto) to guarantee the best adhesion during the UV-gluing, realized with Norland optical adhesive 61.

The device was finally mounted in the vacuum chamber for the experiments, with the openings of the pumping chambers and the gas inlet facing downwards, and connected to the vacuum pumps with flexible tubes secured by a connector block, with a flat viton sealing for preventing possible leakages from the connections. On the top, a plexiglass cover kept the device clamped in its position, as shown in figure A2(c).

A test of the pumping efficiency of the differentially-pumped integrated glass chip was conducted by measuring the pressure in the main chamber for various gas inlet pressures, with the vacuum pumps operating (see main text, figure 1(a)). The results reported in figure A2(d) indicate a good vacuum seal, ensuring a high quantity of gas in the central chamber that is promptly evacuated from the side chambers.

Appendix B. Gas density profile measurements

An assessment of the gas confinement in the differentially-pumped integrated glass chip was made by filling the device with argon and imaging the fluorescence emitted when excited by the NIR driving field with an intensity of 1.9×10^{14} W cm^{-2} (see main text, figure 1(c)). The fluorescence intensity can be correlated to the gas density inside the glass chip [16]. A sketch of the experimental setup is shown in figure B1(a).

The differentially-pumped integrated glass chip is mounted and operated as for the UV generation measurements. The fluorescence is collected outside the vacuum chamber by a 30 cm focal length lens in a 45-degree configuration and sent onto a tube lens ($f = 7$ cm) connected to a CMOS camera (Thorlabs DCC1545M). The residual NIR light is filtered by a band pass filter (Thorlabs FGB37M). This external imaging scheme is possible thanks to the transparency to visible radiation of both the fused silica material of the glass chip and the plexiglass cover of the vacuum chamber. With this setup it was possible to acquire the images reported in figure B1(b), which qualitatively show the effect of the differential pumping in confining the gas in the central part of the cell, when the backing pressure is 0.25 bar. The intensity profiles in

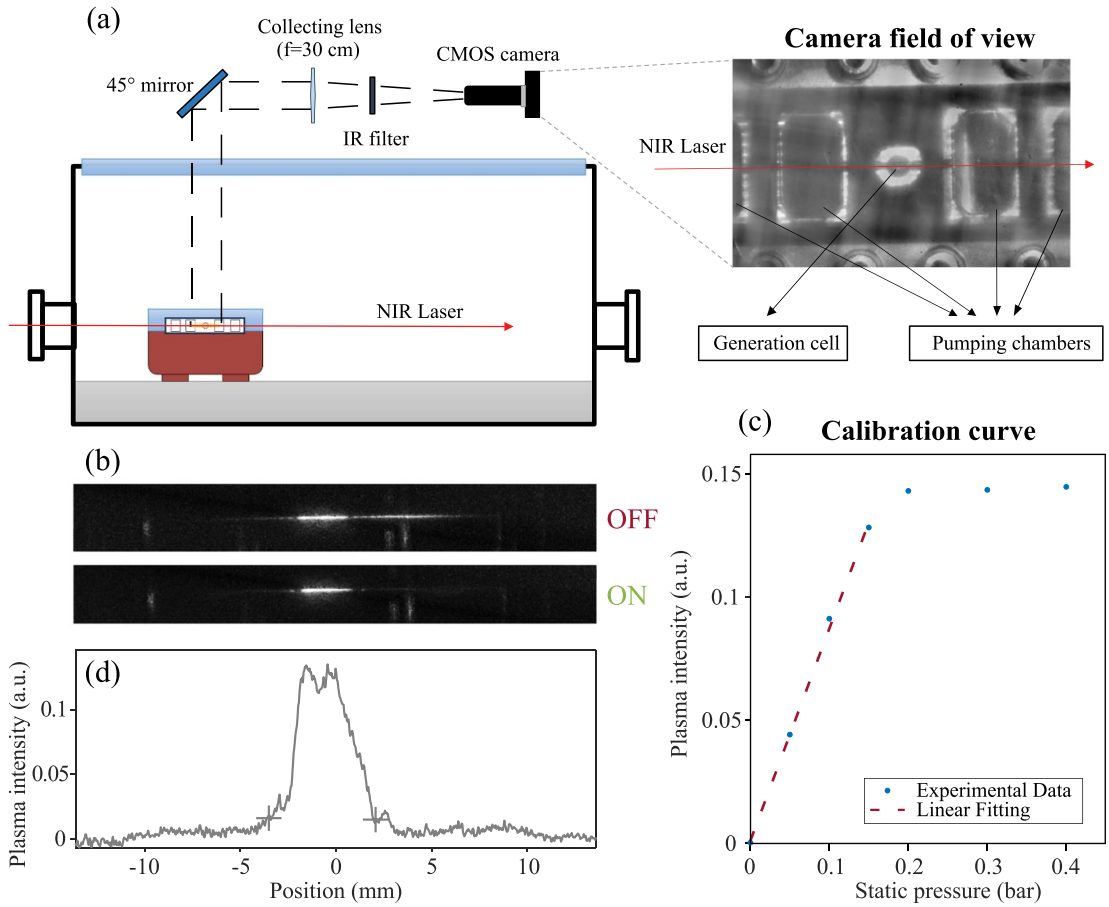

Figure B1. (a) Scheme of the setup for imaging the plasma fluorescence emission from the differential-pumping glass chip. The zoom in shows a camera image of the mounted chip. (b) Camera images of the plasma fluorescence profile along the chip when the differential-pumping is switch off and on, respectively. (c) Calibration curve showing the peak intensity of the plasma fluorescence as a function of the static argon pressure injected into the main vacuum chamber. A linear response is observed for pressures up to 0.15 bar. (d) Fluorescence signal at 0.15 bar input pressure. The crosses mark the beginning and end of the region in which the signal has been extracted to be used as the density profile for the simulations presented in the main text.

figure 1(c) are retrieved from these 2D fluorescence images extracting the intensity of each on-axis pixels and averaging over 10 pixels in the transverse direction both above and below the axis.

While we can obtain some quantitative information on the gas density distribution inside the central cell, such studies are limited to gas pressures lower than the ones used for the UV supercontinua generation. We performed a calibration of the fluorescence in static conditions, filling the vacuum chamber with different gas pressures of argon and imaging the generated plasma inside the glass chip. As shown in figure B1(c), a linear relation holds up to 0.15 bar in the generation cell. For higher pressures the fluorescence intensity no longer increases. This behavior is a consequence of the collective nature of the radiative process. For low pressures the interaction between atoms is negligible and has no influence on the fluorescence intensity. Instead, for high gas densities the decay due to non-radiative processes (induced by i.e. collisions) does not allow to correlate fluorescence intensity and gas density. For our UV generation simulations, the central section of the fluorescence intensity profile measured in the linear regime at 0.15 bar was used (figure B1(d)).

ORCID iDs

Vincent Wanie https://orcid.org/0000-0001-8274-4617
Pasquale Barbato https://orcid.org/0000-0002-3418-5651
Erik P Månsson https://orcid.org/0000-0003-3567-2985
Andrea Trabattoni https://orcid.org/0000-0002-0187-9075
Rebeca Martínez Vázquez https://orcid.org/0000-0001-8728-5819

References

[1] Calegari F and Martin F 2023 Open questions in attochemistry *Commun. Chem.* **6** 184
[2] Wanie V, Colaizzi L, Cartella A, Trabattoni A and Calegari F 2021 Advances of ultraviolet light sources: towards femtosecond pulses in the few-cycle regime *Emerging Laser Technologies for High-Power and Ultrafast Science* ed F Légaré (IOP Publishing Ltd) (https://doi.org/10.1088/978-0-7503-2536-3ch5)
[3] Seka W, Jacobs S D, Rizzo J E, Boni R and Craxton R S 1980 Demonstration of high efficiency third harmonic conversion of high power Nd-glass laser radiation *Opt. Commun.* **34** 469–73
[4] Baum P, Lochbrunner S and Riedle E 2004 Generation of tunable 7-fs ultraviolet pulses: achromatic phase matching and chirp management *Appl. Phys.* B **79** 1027–32
[5] Tan H-S, Schreiber E and Warren W S 2002 High-resolution indirect pulse shaping by parametric transfer *Opt. Lett.* **27** 439–41
[6] Varillas R B, Candeo A, Viola D, Garavelli M, De Silvestri S, Cerullo G and Manzoni C 2014 Microjoule-level, tunable sub-10 fs UV pulses by broadband sum-frequency generation *Opt. Lett.* **39** 3849
[7] Brahms C, Austin D R, Tani F, Johnson A S, Garratt D, Travers J C, Tisch J W G, Russell P S J and Marangos J P 2019 Direct characterization of tuneable few-femtosecond dispersive-wave pulses in the deep UV *Opt. Lett.* **44** 731–4
[8] Travers J C, Grigorova T F, Brahms C and Belli F 2019 High-energy pulse self-compression and ultraviolet generation through soliton dynamics in hollow capillary fibres *Nat. Photonics* **13** 547–54
[9] Brahms C and Travers J C 2022 Soliton self-compression and resonant dispersive wave emission in higher-order modes of a hollow capillary fibre *J. Phys. Photon.* **4** 034002
[10] Reduzzi M *et al* 2023 Direct temporal characterization of sub-3-fs deep UV pulses generated by resonant dispersive wave emission *Opt. Express* **31** 26854
[11] Reiter F, Graf U, Schultze M, Schweinberger W, Schröder H, Karpowicz N, Azzeer A M, Kienberger R, Krausz F and Goulielmakis E 2010 Generation of sub-3 fs pulses in the deep ultraviolet *Opt. Lett.* **35** 2248
[12] Galli M *et al* 2019 Generation of deep ultraviolet sub-2-fs pulses *Opt. Lett.* **44** 1308–11
[13] Wanie V *et al* 2023 Capturing electron-driven chiral dynamics in UV-excited molecules (arXiv:2301.02002)
[14] DeLong K W, Trebino R, Hunter J and White W E 1994 Frequency-resolved optical gating with the use of second-harmonic generation *J. Opt. Soc. Am.* B **11** 2206
[15] Osellame R, Hoekstra H J W M, Cerullo G and Pollnau M 2011 Femtosecond laser microstructuring: an enabling tool for optofluidic lab-on-chips *Laser Photon. Rev.* **5** 442–63
[16] Comby A, Beaulieu S, Descamps D, Petit S and Mairesse Y 2018 Absolute gas density profiling in high-order harmonic generation *Opt. Express* **26** 6001–9
[17] Kolesik M and Moloney J V 2004 Nonlinear optical pulse propagation simulation: From Maxwell's to unidirectional equations *Phys. Rev.* E **70**
[18] Brahms C and Travers J C 2021 A flexible nonlinear optical pulse propagator (available at: https://zenodo.org/records/10323704)
[19] Tani F, Travers J C and Russell P S J 2014 Multimode ultrafast nonlinear optics in optical waveguides: numerical modeling and experiments in kagomé photonic-crystal fiber *J. Opt. Soc. Am.* B **31** 311
[20] Geissler M, Tempea G, Scrinzi A, Schnürer M, Krausz F and Brabec T 1999 Light propagation in field-ionizing media: extreme nonlinear optics *Phys. Rev. Lett.* **83** 2930–3
[21] Perelomov A M, Popov V S and Terent'ev M V 1966 Ionization of atoms in an alternating electric field *Sov. Phys - JETP* **23** 924–34 (available at: www.jetp.ras.ru/cgi-bin/e/index/e/23/5/p924?a=list)
[22] Perelomov A M, Popov V S and Terent'ev M V 1967 Ionization of atoms in an alternating electric field: II *Sov. Phys - JETP* **24** 207–17
[23] Reiter F *et al* 2010 Route to attosecond nonlinear spectroscopy *Phys. Rev. Lett.* **105** 1–4
[24] Ciriolo A G *et al* 2020 High-order harmonic generation in a microfluidic glass device *J. Phys. Photonics* **2** 024005